PERFORMANCE OF AN IMPACT-BASED EARTHQUAKE EARLY WARNING SYSTEM IN THE ALBORAN SEA

Lucía Escudero[1], Aldo Zollo[2], Maurizio Mattesini[1], Raffaele Rea[2], Luca Elia[3], Simona Colombelli[2] and Elisa Buforn[1]

[1] Departamento de Física de la Tierra y Astrofísica, Universidad Complutense de Madrid, Plaza de Ciencias 1, 28040 Madrid (Spain).

[2] Dipartimento di Fisica "*Ettore Pancini*", Università degli Studi di Napoli Federico II, Via Cintia, 21, 80126 Naples (Italy).

[3] Istituto Nazionale di Geofisica e Vulcanologia, Sezione di Napoli Osservatorio Vesuviano, Naples (Italy).

Maurizio Mattesini and Elisa Buforn **also at** Facultad de Ciencias Físicas, Instituto de Geociencias (UCM-CSIC), Plaza de Ciencias 1, Madrid E-28040 (Spain).

Correspondig author: Lucía Escudero, *Dpt. Física de la Tierra y Astrofísica, Universidad Complutense, Plaza de Ciencias 1, 28040, Madrid (Spain), e-mail:* lescud01@ucm.es.

Abstract:

This paper presents the implementation and testing of a new P-wave shaking-forecast-based early warning system (EEWS) at the Ibero-Maghrebian Region (IMR). The method integrates PGV predictions derived from observed P-wave amplitudes with region-specific ground motion prediction equations to facilitate real-time mapping of the potential damage zone. We determined empirical relationships between PGV and P-wave peak amplitudes (in acceleration, velocity, and displacement) and magnitude, along with the development of a GMPE for $M_w \geq 4$ earthquakes in the IMR. These relationships are validated in the EEWS application using data from the 2016 Alboran Sea seismic series (M_w 5.0–6.4), which showed minimal discrepancies in origin time, epicenter location, and magnitude estimates compared to previous studies. A retrospective

performance analysis for the M_w 6.4 main shock indicated lead-times of 14 to 62 seconds at a PGV threshold of 0.20 cm/s, with lead-times increasing with distance. At a higher threshold of 0.60 cm/s, the lead-time was 20 seconds for distances up to 170 km. The accuracy of impact predictions improved over time, with successful alerts rising from 72% to 90% as the final predictions were made. Despite some limitations due to focusing on moderate-magnitude earthquakes ($M_w \leq 6.4$), the EEWS method has proven effective for offshore events in areas with sparse instrumentation.

Introduction

Population growth and infrastructure concentration in metropolitan areas have increased the vulnerability of society to earthquakes. Earthquakes Early Warning Systems (EEWS) are one of the most effective tools to prevent and mitigate damage caused by earthquakes. These systems can evaluate the destructive potential of an earthquake in real time and issue an early warning that allows the initiation of emergency protocols or the evacuation of vulnerable areas before the arrival of stronger seismic waves, helping to protect the population and infrastructure while mitigating damage (Zollo *et al.,* 2023; Rea *et al.,* 2024).

EEWS have been implemented in seismically active regions, tailored to local seismicity and infrastructure needs (Rea *et al.,* 2024). Operational systems distributing public alerts include Mexico's SASMEX (Espinosa-Aranda *et al.,* 1995; Suarez *et al.,* 2021), Japan's EEWS (Hoshiba *et al.,* 2008), Taiwan's system (Hsiao *et al.,* 2011), and South Korea's system (Sheen *et al.,* 2017). Other systems are in place in Vrancea (Romania) (Clinton *et al.,* 2016), Korokke (India) (Chamoli *et al.,* 2019), the U.S. west coast (Allen and Kanamori, 2003; Böse *et al.,* 2013), and Istanbul (Turkey) (Alcik *et al.,* 2011). Alerts also target specific groups like emergency services. In Italy (Irpinia region) (Satriano *et al.,* 2011; Zollo *et al.,* 2023), China (Peng *et al.,* 2011), Switzerland (Massin *et al.,* 2021), and Chile (Medina *et al.,* 2022), EEWS have been developed for research but do not provide public alerts.

EEWS can adopt either a *network-based* or *onsite* approach. The network-based configuration receives real-time information from seismic sensors deployed in the source epicentral area. This allows automatically identifying the P-wave arrival and define a specific signal time window to calculate the hypocenter and magnitude of the detected earthquakes. This approach uses Ground Motion Prediction Equations (GMPE) to predict ground motion by employing region-specific empirical attenuation relationships (Zollo *et al.,* 2023; Rea *et al.,* 2024). On the other hand, onsite EEWSs use a stand-alone station, or arrays of sensors deployed near the site to be protected. The initial P-wave amplitude is used to estimate the amplitude of other waves (S or surface), without requiring the location and magnitude of the earthquake (Zollo *et al.,* 2023; Rea *et al.,* 2014).

Most recently, Zollo *et al.,* (2023) proposed a new EEWS methodology combining network-based and onsite approaches. It estimates main source parameters (Satriano *et al.,* 2008 for location, Zollo *et al.,* 2023 for magnitude) and predicts Peak Ground Velocity (PGV) using observed P-wave amplitudes and region-specific GMPE, with updates to location and magnitude. The method issues alerts when ground shaking exceeds a user-set threshold, based on a time-evolving P-wave-derived shakemap. A real-time map of the Potential Damage Zone (PDZ) is generated, when Instrumental Intensity (I_{MM}), calculated in terms of PGV, exceeds a defined threshold (Zollo *et al.,* 2023).

In October 2015, the Department of Earth Physics and Astrophysics at *Universidad Complutense de Madrid* (UCM) installed an EEWS using *PRESTo* software (Satriano *et al.,* 2011). It employs a network-based approach adapted to the Ibero-Maghrebian Region (IMR) (Carranza *et al.,* 2013, 2016, 2017, 2021), covering southern Iberia and northern Morocco and Algeria, a tectonically complex zone at the Eurasian-African plate boundary (Fig. 1). This region has experienced major earthquakes like Lisbon 1755, Torrevieja 1829, and Arenas del Rey 1884 (Mézcua and Martínez-Solares, 1983; Buforn et al., 2015). While seismic activity was moderate in the 20th century, it has risen in the last 30 years, with notable events such as Al Hoceima 2004 (M_w 6.4; Stich *et al.,* 2005), Lorca 2011 (M_w 5.1; Pro *et al.,* 2014), and Alboran Sea 2016 (M_w 6.4; Buforn *et al.,* 2017), some causing significant damage. The expected seismic hazard level for a 475-year return period in the southern Iberian Peninsula and areas near the Alboran Sea ranges from 0.04 g to 0.24 g (IGN, 2013) corresponding to I_{MM} = VI and VIII, respectively (Faenza and Michelini, 2010).

The results of the EEWS installed at UCM show its viability for the IMR (Carranza, 2016; Carranza *et al.,* 2017 and 2021). Nonetheless, to enhance performance, the methodology proposed by Zollo *et al.,* (2023) has been implemented at UCM, adapting it to the seismic characteristics of the IMR. This new setting uses the *QuakeUp* software that implements the shaking-forecast based early warning methodology described in Zollo *et al.,* (2023), as developed by the *RISSC-Lab Unità di RIcerca in Sismologia Sperimentale e Computazionale* of *Università degli Studi di Napoli Federico II.*

The effectiveness of *QuakeUp* has already been demonstrated with both large-magnitude (Rea *et al.,* 2024) and moderate-magnitude earthquakes (Zollo *et al.,* 2023), although these tests have been performed in conditions of densely instrumented areas. The main purpose of this work is to study the behavior of *QuakeUp* in a region with lower instrumentation density during moderate-magnitude offshore earthquakes recorded by inland stations. To achieve this aim, we performed an offline retrospective analysis of the early warning method during the main shock (M_w 6.4; Fig. 1) and the six $M_w \geq 5$ earthquakes from the 2016 seismic sequence in the Alboran Sea. Several researchers (Buforn *et al.,* 2017; Gràcia *et al.,* 2019) have performed comprehensive studies on this sequence, providing a robust observational dataset of waveform data to evaluate *QuakeUp*'s performance. In this paper, we will utilize the relocations and focal mechanisms from Buforn *et al.,* (2017) for the main shock, foreshock (FOR), and aftershocks (AS) with $M_w \geq 5$ (Fig. 1). The data include three-component velocity records from 38 seismic stations located at the IMR (epicentral distances < 700 km), sourced from the seismic networks of the Instituto Geográfico Nacional (IGN), Western Mediterranean (WM), and the Instituto Português do Mar e da Atmosfera

(IPMA) (Fig. 1). Additionally, we will assess the system's performance for the main shock in terms of correct and failed alerts based on various PGV/I_{MM} thresholds and PDZ.

Methodology

The *QuakeUp* approach combines earthquake detection and location, magnitude estimation, and PGV prediction. The process used to obtain these parameters is briefly described below, with the block diagram of the method shown in Figure 2. More details can be found in Zollo *et al.,* 2023.

QuakeUp uses the velocity components from the 38 broad-band stations (Fig. 1). Displacement traces are obtained through integration, followed by a high-pass Butterworth filter (cut-off at 0.075 or 1 Hz, as per Caruso *et al.,* 2017) to remove low-frequency drifts and baselines from the integration process, while acceleration traces are obtained through differentiation without filtering. The P-wave arrival is identified on the vertical components using the Filter-Picker 5 algorithm (Lomax *et al.,* 2012). When the earthquake is detected at 5 stations, the first estimate of the hypocenter location and origin time is provided using the RTLOC algorithm (Satriano *et al.,* 2008). This time is referred to as T_{FIRST}. The hypocenter location and origin time value are updated as the P-wave arrival is identified at more stations. To minimize the noise dominant effect of stations at large epicentral distances, we set *QuakeUp* to only use records from stations within 400 km of the first station that detects earthquakes (EALB in Fig. 1).

Peak amplitudes of P-waves are measured at each station, as the absolute maximum amplitude values of the P-wave on the vertical component of acceleration, velocity, and displacement records (P_a, P_v, and P_d, respectively). These values are measured in an expanded time window that grows by an interval of 0.5 s up to 20 s from the first P-wave arrival time (Zollo *et al.,* 2023).

The moment magnitude (M_w) is determined from an empirical relationship (Eq. 1) between the hypocentral source-to-receiver distance (R) and the measured P-wave peak amplitude parameters:

$$M_w^x(P_x, R) = A_x + B_x \log_{10} P_x + C_x \log_{10} R \tag{1}$$

where the subindex x=a, v, d refers to acceleration, velocity and displacement, respectively; R is the hypocentral distance measured in km and A_x, B_x, C_x are region-specific coefficients obtained through linear regression. At each station, the calculated M_w^x (P_x, R) values are averaged at each time step. Thus, the earthquake magnitude is the average of the magnitudes calculated at all stations on expanding time windows. The time at which the calculated M_w reaches its *plateau* value is referred to as T_{STB}.

In this work, the IMR-specific coefficients for Eq. (1) have been calculated. For this purpose, we have selected 15 earthquakes that occurred in the IMR between 2000 and 2024, with $4.4 \leq M_w \leq 6.8$ (Table S1; Fig. S1). A total of 1095 velocity records were available from seismic stations at hypocentral distances ranging from 40 to 700 km (Text S1). Empirical relations (Eq. 1) were then derived for P-wave time windows of 10 and 20 s and used in *QuakeUp*. At each time instant, if the P-wave time window is less than 10 s, the coefficients for the 10 s window are used, while if it is between 10 and 20 s, the coefficients for the 20 s window are applied.

Figure 3a shows the values of P_x (where x = a, v, d) for 20 s P-wave time window of the selected earthquakes (Text S1). Table 1 presents the IMR-specific coefficients for Eq. (1), together with the standard deviation of the fits, for 20 s P-wave time windows. The solid line in Figure 3a shows the regression law, with uncertainty indicated by the dashed line, for a hypocentral distance of 350 km, half of the maximum observed distance. For comparison, Figure S2a and Table S2 illustrate the interpolation law and parameters for the of 10 s time window case.

The PGV value is predicted at the recording stations from P-wave amplitudes using an empirical relation (Eq. 2) based on the measured P_x (x = a, v, d) values, as follows:

$$\log_{10}\mathrm{PGV}(\mathrm{P_x}) = \mathrm{A'_x} + \mathrm{B'_x}\log_{10}\mathrm{P_x} \qquad (2)$$

where $\mathrm{A'_x}$ and $\mathrm{B'_x}$, are region-specific coefficients obtained through linear regression. At every station, the PGV(P_x) values derived from Eq. (2) are averaged at each time step. Furthermore, the predicted PGV from the vertical P_x amplitude (Eq. 2) at each recording station is continuously compared to the PGV measured on the horizontal components. At any given time, the maximum between these two values is used as the peak ground motion estimate (Zollo *et al.,* 2023).

IMR-specific coefficients for Eq. (2) were derived using the geometric mean of horizontal PGV values from the same database as Eq. (1) (Text S1). The coefficients of Eq. (2) are calculated using linear regression with the P_x values (where x = a, v, d) in 10 and 20 s time windows (Table 2; Table S3). Figure 3b shows PGV values for selected earthquakes (Text S1) versus P_x values in 20 s P-wave windows, with Figure S2b presenting results for 10 s windows. This method also allows the calculation of PGV at locations for which no observations are available (virtual nodes) and at recording stations where the P-wave has not been identified. At each time step, the PGV prediction is generated using the physics-based interpolation algorithm, implemented in USGS ShakeMap software (Worden *et al.,* 2010). Therefore, *QuakeUp* combines the available information from recording stations (PGV values, onsite approach) with regional GMPE and real-time estimates of earthquake location and magnitude (network-based approach) (Zollo *et al.,* 2023).

The GMPE proposed by Picozzi *et al.,* (2015) for the IMR is used here, which is inferred from a waveform database of 119 earthquakes that occurred in the IMR between 2006 and 2011 (Carranza, 2013). The maximum magnitude used in this database is M_w 6.4, corresponding to the 2004 Al-Hoceima earthquake (Fig. 1; Cakir *et al.,* 2004; Stich *et al.,* 2005), while many of the records (35%) correspond to events with magnitudes smaller than $M_w = 4.0$ (Carranza, 2013). Therefore, given the larger number of earthquakes with $M_w \leq 4.0$ in this database compared to those of greater magnitude, a specific GMPE was developed for this study (Text S2). With this aim, twenty-eight earthquakes that occurred in the IMR between 2000 and 2024, with $4.0 \leq M_w \leq 6.8$, were selected (Table S4; Fig. S3). The outcome of such an *ad hoc* refinement is expressed by the following simplified GMPE (Eq. (3)):

$$\log_{10}\mathrm{PGV} = -2.74 + 0.99\ \cdot\ \mathrm{M_w} - 1.78\ \cdot \log_{10}\mathrm{R} \qquad (3)$$

where PGV is measured in cm/s and R is the hypocentral distance in km. This result is significant as it enables PGV prediction based on time and distance from the seismic source. While time is not explicit in the equation, it is implicit through time-dependent changes in earthquake magnitude (Eq. 1).

The PGV values were further converted into I_{MM} by using the empirical relationship of Faenza and Michelini (2010) (MCS scale). As a result, a shakemap in terms of I_{MM} is generated and updated over time, allowing for the monitoring of the PDZ. The method is time-evolving, as the shape of the PDZ is modelled based on new data received from progressively distant stations, and larger P-wave windows are integrated into the EEWS system (Zollo *et al.,* 2023).

For each station, I_{MM}^{pred} is the I_{MM} value calculated from PGV estimated by *QuakeUp* (Eq. 2 and 3). The observed PGV is the geometric mean of the two maximum horizontal ground motion velocity values. I_{MM}^{obs} is computed from this observed PGV. Lead-time is the time between when I_{MM}^{pred} exceeds the user-defined intensity threshold (I_{MM}^{thres}) and when I_{MM}^{obs} reaches the same threshold. The maximum observed intensity of the 2016 Alboran seismic series is VI (EMS-98), according to the IGN catalogue. Two operational PGV thresholds were used: 0.20 cm/s (I_{MM}^{thres} = IV) and 0.60 cm/s (I_{MM}^{thres} = V) (Faenza and Michelini, 2010).

The accuracy of impact prediction using the EEWS method is assessed by comparing I_{MM}^{obs} and I_{MM}^{pred} in terms of whether they exceed a user-defined threshold, I_{MM}^{thres}. By applying the decision matrix of Zollo *et al.,* (2023), the number of Successful Alerts (SA), Successful No-Alerts (SNA), Missed Alerts (MA), and False Alerts (FA) can be assessed:

$$\text{SA: } I_{MM}^{pred} \geq I_{MM}^{thres} \ \& \ I_{MM}^{obs} \geq I_{MM}^{thres}$$

$$\text{SNA: } I_{MM}^{pred} < I_{MM}^{thres} \ \& \ I_{MM}^{obs} < I_{MM}^{thres}$$

$$\text{MA: } I_{MM}^{pred} < I_{MM}^{thres} \ \& \ I_{MM}^{obs} \geq I_{MM}^{thres}$$

$$\text{FA: } I_{MM}^{pred} \geq I_{MM}^{thres} \ \& \ I_{MM}^{obs} < I_{MM}^{thres}$$

The Time of the First Alert (TFA) is defined as the time when, for the first time, the value of $\mathrm{I}_{\mathrm{MM}}^{\mathrm{pred}}$ at one of the recording stations (Fig.1) exceeds the previously established $\mathrm{I}_{\mathrm{MM}}^{\mathrm{thres}}$. The Blind Zone is the region where, due to its proximity to the epicentre, it is not possible to provide a warning before the arrival of the most destructive waves (Carranza, 2016). This occurs when $\mathrm{I}_{\mathrm{MM}}^{\mathrm{thres}}$ is observed at the recording station ($\mathrm{I}_{\mathrm{MM}}^{\mathrm{obs}} \geq \mathrm{I}_{\mathrm{MM}}^{\mathrm{thres}}$) before *QuakeUp* can predict it ($\mathrm{I}_{\mathrm{MM}}^{\mathrm{pred}} < \mathrm{I}_{\mathrm{MM}}^{\mathrm{thres}}$).

Results

The performance of *QuakeUp* in IMR has been evaluated in terms of speed of warning and the goodness of the impact prediction, for the main shock, M_w 6.4, and the foreshock and aftershocks, M_w 5.0 - 5.2, of the 2016 Alboran Sea seismic series. The hypocentral location, origin time and M_w calculated by *QuakeUp* are compared with those of Buforn *et al.,* (2017). Differences in origin time (ΔOT), epicentre location (ΔR), depth (Δh) and magnitude (ΔM_w) between the two studies are calculated.

Performance of EEWS during the main shock

The main shock (M_w 6.4, black star, Fig. 1) on 25 January 2016 had a hypocenter at (35.63°N, 3.75°W) and a depth of 7 km (Buforn *et al.,* 2017). The origin time (OT) used for this earthquake is the one proposed earlier by Buforn *et al.,* (2017), which is 04.22:00.40.

Figure 4a-c shows the values of ΔOT, ΔR, and Δh for the main shock, while Figure 4d illustrates the calculation of M_w made by *QuakeUp*. The first estimation of all these parameters by *QuakeUp* is performed 23.11 s after the OT (T_{FIRST}) using 5 stations. The final estimate of these parameters is made 75.5 s after the OT, by using a total of 23 stations. The values of ΔOT (Fig. 4a) and ΔR

(Fig. 4b) are consistently less than 2 s and 10 km, respectively. Overall, location results are quite stable in time. Figure 4c shows Δh = 63 km at T_{FIRST}. However, one second later, this value drops to 20 km. Throughout the rest of the simulation, Δh fluctuates between 20 and 18 km, with 18 km being the value in the final estimate.

The magnitude is estimated at each station from Eq. (1) at each instant (grey curves, Fig. 4d) and then averaged over time (blue curve, Fig. 4d), resulting in the calculated M_w value for the earthquake. At T_{FIRST}, *QuakeUp* calculates an M_w value of 6.3, which decreases to 6.0 in 1 s, and then varies between 6.0 and 6.1 for the next 17 s. The magnitude reaches a *plateau* value of 6.1 at 41.11 s after OT (T_{STB}).

A similar behaviour of M_w is observed at all stations (grey curves, Fig. 4d). There is an initial increase in M_w during the first 6-8 s of P-wave recording, until a *plateau* value is reached. Despite the similar trend, the magnitude curves at different stations exhibit variability due to factors such as azimuthal location, site conditions, and propagation effects, not accounted for in the empirical relationship (Eq. 1) (Rea *et al.,* 2024). The distribution of the magnitude estimates at the stations at the final estimate is shown in the histogram on the left side of Figure 4d. The mean value of this distribution is 6.1, with a standard deviation of 0.3.

Figure 5 shows lead-time (vertical black lines) as a function of epicentral distance for I_{MM}^{thres} = IV and V. Green circles indicate when I_{MM}^{pred}=IV and V are first reached at 11 stations (Fig. 5a) and 5 stations (Fig. 5b), respectively, while red circles show when I_{MM}^{obs} reaches the threshold. The TFA for both thresholds is OT + 23.11 s. *QuakeUp* predicts that I_{MM}^{thres}=IV will be exceeded up to 260 km from the epicenter (Fig. 5a), and I_{MM}^{thres}=V up to 170 km (Fig. 5b). Considering both thresholds, stations within 80 km are in the blind zone (more details in the Discussion Section). For stations outside this zone, lead-time for I_{MM}^{thres}=IV ranges from 14 to 62 s, generally increasing with distance, and is 20 s for I_{MM}^{thres}=V at 3 stations.

In Figure 6, the impact prediction maps for I_{MM}^{thres} = IV (Faenza and Michelini, 2010) are presented at three different times: the TFA (OT + 23.11 s, Fig. 6a), the time when *QuakeUp* last calculates I_{MM}^{pred} at the stations (OT + 105.67 s, Fig. 6c), and an intermediate time (OT + 63.56 s, Fig. 6b). Additional details for I_{MM}^{thres} = V can be found in Text S4.

In Figure 6a, at TFA, successful alerts (SAs + SNAs: 74%, green triangles) outnumber missed and false alerts (MAs + FAs: 26%), with MAs and FAs mainly near the Alboran Sea and SE Iberia (280–390 km from the epicenter). By 63.56 s after OT (Fig. 6b), successful alerts increase to 86%, with all MAs in SE Iberia and one FA. At 105.67 s after OT (Fig. 6c), successful alerts reach 89%, with no FAs but persistent MAs in SE Iberia. The I_{MM}^{pred} values at these stations remain below the threshold due to their azimuthal location, a topic explored further in the Discussion Section.

At the same time instant, when considering I_{MM}^{thres} = V (Text S4, Fig. S5) instead of IV, the number of successful alerts (SAs + SNAs) increases by about 8-15%. In addition, the number of MAs and FAs decreases by approximately 8-15% (see Fig. S6).

Performance of the EEWS for the foreshock and aftershock of the 2016 Alboran Sea seismic series

Figure 7a-d shows the values of ΔOT, ΔR, Δh, and ΔM_w for the foreshock and aftershocks (M_w 5.0-5.2, FOR and AS1-5, Fig.1) of the 2016 Alboran seismic series. The differences between I_{MM}^{pred} and I_{MM}^{obs} at the recording stations (ΔI_{MM}) are also calculated. These differences are measured at two-time instants: T_{FIRST} and T_{STB} (Table S5 and S6). For these earthquakes, T_{FIRST} is observed between 23.19 s (FOR) and 24.18 s (AS2), and T_{STB} between 39.38 s (FOR) and 56.07 s (AS5) after the origin time calculated by Buforn *et al.,* (2017) (Table S5; Text S3).

In Figure 7a, it is observed in T_{FIRST} that $-4\ s \leq \Delta OT \leq 0.5\ s$, while in T_{STB}, the differences are reduced to $0\ s \leq \Delta OT \leq 2.5\ s$. Regarding the location of the hypocenters, in T_{FIRST}, 67% of the earthquakes have $\Delta R \leq 20$ km (Fig. 7b) and $\Delta h \leq 30$ km (Fig. 7c). The remaining earthquakes show $\Delta R \geq 30$ km (AS2 and AS3) and $\Delta h \geq 60$ km (AS3 and AS4). In T_{STB}, all earthquakes have $\Delta R \leq 12$ km, and all hypocenters are deeper than those calculated by Buforn *et al.,* (2017) [12 km (AS3) $\leq \Delta h \leq$ 25 km (AS4)]. In T_{FIRST}, *QuakeUp* calculates a value of M_w higher than that determined by Buforn *et al.,* (2017) for all earthquakes ($0.2 \leq \Delta M_w \leq 1.1$, Fig. 7d), while in T_{STB}, these differences are reduced to $-0.1 \leq \Delta M_w \leq 0.2$ (Fig. 7d).

Figure 7e shows that, at T_{FIRST}, $\Delta I_{MM} = 0$ in 41.21% of the stations. A difference of $\Delta I_{MM} = 1$ is found in 30.65% of the stations, while higher differences ($2 \leq \Delta I_{MM} \leq 4$) are observed in the remaining stations. In T_{STB}, the percentage of stations with $\Delta I_{MM} = 0$ increases to 60.80%. At this point, $\Delta I_{MM} = -1$ is observed for 3.02% of stations, and the percentage of stations with $1 \leq \Delta I_{MM}$ decreases significantly to 9.04%.

Discussion

The performance of an EEWS based on the progressive temporal prediction of ground motion ('shaking') has been studied for the $M_w \geq 5$ earthquakes of the 2016 Alboran seismic series (Fig. 1), using velocity records from broadband stations within the IMR, which cover the areas of highest seismic risk in the region (IGN, 2013).

In this work, we tested different P-wave time window lengths. Initially, a maximum 10 s window was used to include the two peaks observed in the source time function of the main shock (occurred at 3 s and 10 s; Buforn et al., 2017). However, using a time window of 10 s, magnitude values were systematically underestimated. To avoid this problem, we tested different time window lengths, ranging from 10 s to 25s. The best results for magnitude estimation were obtained with a time window of 20 s. Given that most recording stations are located far from the events' hypocenters (30 of the 38 stations used are located between 170 and 700 km from the epicenter, Fig. 1), the chosen time window (20 s) should not include the S-waves. Moreover, for such long distances we have to consider the effect of anelastic attenuation, which tends to lengthen the P-wave phase in the signal (Udías and Buforn, 2018). Extending the window to 20 s yielded source parameters closer to those reported by Buforn et al., (2017), improving magnitude estimates, which are crucial for precise and rapid impact predictions, enabling effective alerts.

The system's performance for the main shock has been evaluated based on the quickness of issuing an alert and the accuracy of impact prediction at recording stations. For the sake of clarity, the most important results (in **bold**) are highlighted below, followed by a concise explanation.

- **The extension of the blind zone is 80 km from the epicenter for both thresholds ($\mathbf{I_{MM}^{thres}}$=IV and V).** This is related to the inhomogeneous station distribution within the epicentral area used in this study (Fig. 1). Inside the blind zone there are only two stations: EALB and WMELI (Fig. 1), as well as cities such as Al-Hoceima, Imzouren and Melilla (Fig. 8). Increasing the number of stations (especially along the Moroccan coast) or deploying Ocean-Bottom Seismometers would enable earlier localization of the earthquake, reducing the blind zone.

- **The lead-time for stations outside the blind zone ranges from 14 to 62 s for $\mathbf{I_{MM}^{thres}}$=IV and is 20 s for $\mathbf{I_{MM}^{thres}}$=V.** The best performance is achieved with $\mathrm{I_{MM}^{thres}}$=IV, as it allows predicting ground motion at stations up to 260 km (Fig. 5a). Additionally, the 20 s lead time for $\mathrm{I_{MM}^{thres}}$=V at stations up to 170 km (Fig. 5b) is equal to or shorter than that obtained with $\mathrm{I_{MM}^{thres}}$=IV (Fig. 5a). Therefore, the lower threshold ensures earlier alerts and maximizes response time.
- **The choice of the intensity threshold affects the speed at which alerts are issued.**
  - For **$\mathbf{I_{MM}^{thres}}$=IV** (Fig. 5a), at TFA, stations already reached by the P-wave (epicentral distance < 150 km) do not require a long P-wave window to accurately predict the shaking level ($\mathrm{I_{MM}^{pred}} \geq$ IV). Even at the recording stations not yet reached by the P-wave (GMPE-predicted PGVs), a reliable alert can still be issued, resulting in lead-times ranging from 14 to 62 s.
    - The GMPE-predicted PGVs are based on the M_w value in TFA (6.3, Fig. 4d). For instance, if *QuakeUp* had calculated M_w=6.1 during offline testing (plateau value, Fig. 4d; Text S5), GMPE-predicted PGVs would not estimate the shaking level at stations beyond 200 km, relying on onsite prediction and reducing lead time (Fig. S7a). If the computed M_w value had been 5.8 (6.1 – 0.3, Fig. 4d), GMPE-based-$\mathrm{I_{MM}^{pred}}$ would never exceed the threshold, making lead time fully dependent on onsite prediction (Fig. S7b). Conversely, if the estimated M_w had been 6.4 (6.1 + 0.3) would yield the same behavior as M_w=6.3 (Fig. S7c; Fig. 5a).

    - For $\mathbf{I_{MM}^{thres}}$=V (Fig. 5b), *QuakeUp* relies on the P-wave reaching the station (Eq. 2) to predict that I_{MM}^{pred} will exceed the threshold, resulting in shorter lead times (20 s).

- **The quality of EEWS's strong shaking predictions is affected by the choice of $\mathbf{I_{MM}^{thres}}$.** For a specific time, using I_{MM}^{thres}=V (Fig. S5) instead of IV (Fig. 6) maximizes the ratio of successful alerts to missed and false alerts (Fig. S6). *QuakeUp* improves prediction quality over time, as wider P-wave time windows are recorded at an increasing number of stations.
    - Modifying M_w in the TFA would alter the corresponding impact prediction map (Text S5, Fig. S8). If the M_w value had been lower (6.1 or 5.8), the number of MAs would have increased, especially as M_w decreased. This occurs because at stations beyond 150 km (not yet reached by the P-wave), I_{MM}^{pred} from GMPE-predicted PGVs (Eq. 3) would not exceed the threshold. Conversely, a higher M_w (6.4) would reduce the number of MAs. The temporal evolution of the impact maps with different M_w values during offline testing converges to the map in Figure 6c, as I_{MM}^{pred} eventually exceeds the threshold at the same stations, either earlier or later (Fig. S7), ensuring the same number of correct alerts.
- **At stations located on a nodal plane, the MAs persist over time.** The MS rupture plane has a strike of 30º, a dip of 87º and a slip of 26º (Fig. 1). Stations located at the nodal plane have small P-wave amplitude (P-wave radiation pattern ranging from 0.08 to 0.25) while the high-frequency, large amplitude directivity effect carried by S-waves is significant. So, it is not possible to accurately predict the observed shaking level (Eq. 2). This limitation could be overcome by estimating the focal mechanism or fault orientation in real-time with early P and S-wave signals (Böse *et al.,* 2012; Wang *et al.,* 2024).

We have estimated the differences between $\mathrm{I}_{\mathrm{MM}}^{\mathrm{pred}}$ and $\mathrm{I}_{\mathrm{MM}}^{\mathrm{obs}}$ at the stations (Fig. 7d). We define an acceptable margin of error as $|\Delta \mathrm{I}_{\mathrm{MM}}| \leq 1$. From the obtained results for foreshock (FOR) and aftershock (AS1-5, Fig. 1), we observed the following:

- ***QuakeUp* correctly predicts the observed shaking levels for moderate-magnitude earthquakes ($5.0 \leq M_w \leq 5.2$).** In T_{FIRST}, 71.86% of the stations fall within this margin, rising to 90.96% in T_{STB}. In both instants, $|\Delta \mathrm{I}_{\mathrm{MM}}| > 1$ occurs at stations not yet reached by the P-wave, where $\mathrm{I}_{\mathrm{MM}}^{\mathrm{pred}}$ overestimates $\mathrm{I}_{\mathrm{MM}}^{\mathrm{obs}}$ due to an overvaluation of the magnitude (Fig. 7d).

It is important to remark that *QuakeUp* is an impact-based EEWS method, and its primary goal is not the optimal determination of source parameters but rather the accurate and rapid prediction of shaking level. However, these parameters are essential for precise impact predictions at non-instrumented sites (Eq. 3). Thus, accurate determination is advisable.

- ***QuakeUp* provides highly accurate estimates of earthquake source parameters.** At T_{STB}, for all analyzed earthquakes, *QuakeUp* achieves $\Delta \mathrm{OT} \leq 2$ s, $\Delta R \leq 20$ km and $|\Delta \mathrm{Mw}| \leq 0.3$ (Fig. 4 and 7) according to the error criteria proposed by Carranza (2016) for the IMR. Values of $12 \text{ km} \leq \Delta h \leq 25$ km (Fig. 4c and 7c) could be reduced with enhanced azimuthal coverage from additional stations in North Africa (Carranza, 2016).
- **No influence of focal mechanism on source parameter estimation.** The 2016 Alboran seismic series present different types of focal mechanisms. The FOR, MS, and AS1-2

events have strike-slip mechanisms, and AS3-5 show pure thrusting faulting mechanisms (Fig. 1). The change in focal mechanisms does not affect the values of ΔOT, ΔR, Δh and ΔM_w.

Figures 8a-c show the snapshots of the shakemap for the main shock (see Video S1) at different times after OT, reported in each panel. If we consider I_{MM}^{thres}=V, (green areas in Fig. 8a-c), associated with the potential impact levels of "moderate" and "very light" damage (Faenza and Michelini, 2010), the PDZ refers to areas (bounded by black isolines in Fig. 8a-c) where I_{MM}^{pred} exceeds this threshold.

- **The PDZ expands over time, changing as new P-wave data propagates across the array.** The PDZ is initially shown only in North Africa, while at later times, it extends to SE Iberia (Fig. 8a-c). In North Africa, the PDZ remains nearly circular as it expands up to 100 km from the epicenter, due to limited station coverage (Fig. 1) it is controlled by the GMPE-predicted PGV.
- **A precautionary first alert could be issued for the areas surrounding the Alboran Sea at TFA.** This includes the municipalities of Al-Hoceima and Imzouren, for which *QuakeUp* subsequently calculates I_{MM}^{pred} = VI (1 and 2 in Fig. 8b-c). As *QuakeUp* refines the I_{MM}^{pred} calculations, the alert could be extended to municipalities further away from the seismic source, up to 170 km, where the I_{MM}^{thres} would eventually be exceeded (Fig. 5b).

Figure 8d represents the observed intensity map (EMS-98) of the main shock taken from the IGN Seismic Catalog (see Data and resources), covering both sides of the Alboran Sea, including Ceuta and Melilla cities. As the shakemaps (Fig. 8a-c) use MCS scale, we carry out a a qualitative comparison between the final shakemap (OT + 96.52 s; Fig. 8c) and the observed intensity map (Fig. 8d). This comparison shows a satisfying match. For instance, for the municipalities of Adra (Almería) and Salobreña (Granada) (4 and 5 in Fig. 8), *QuakeUp* estimates $\mathrm{I}_{\mathrm{MM}}^{\mathrm{pred}}$=V (MCS scale, Fig. 8c), comparable to the observed intensity IV (Fig. 8d), associated with a moderate vibration level (EMS-98). For Melilla (3 in Fig. 8), the IGN assigns intensity VI, indicating a "moderate" impact level with "light" potential damage (EMS-98, Fig. 8d), comparable to $\mathrm{I}_{\mathrm{MM}}^{\mathrm{pred}}$=V-VI (Fig. 8c). This comparison has not been possible for northern Morocco due to the unavailability of intensity values.

Conclusions

In this study, we implemented and tested a new P-wave shaking-forecast-based EEWS called *QuakeUp* at the IMR. This approach uses PGV predictions from observed P-wave amplitudes, combined with region-specific GMPE, for real-time mapping of the PDZ. Key findings include:

- Established relationships for the IMR between PGV and P-wave peak amplitudes (acceleration, velocity, displacement), as well as between magnitude and P-wave amplitudes. A GMPE for $M_w \geq 4$ earthquakes in the IMR was developed.

- These relationships were validated using data from the 2016 Alboran Sea seismic series (M_w 5.0–6.4). Comparisons with Buforn *et al.,* (2017) showed discrepancies of less than 2 s in origin time, less than 12 km in epicenter location, and less than 0.3 in M_w estimation.
- Retrospective analysis of the method's performance for the M_w 6.4 main shock revealed lead-times of 14 to 62 s at I_{MM}^{thres} = IV (PGV = 0.20 cm/s), increasing with epicentral distance (up to 260 km). At I_{MM}^{thres} = V (PGV = 0.60 cm/s), the lead-time was 20 s for distances up to 170 km.
- The accuracy of impact predictions improved over time; for I_{MM}^{thres} = IV, successful alerts increased from 72% at the first alert to 90% at *QuakeUp*'s final prediction.

While our results are somewhat limited to moderate-magnitude earthquakes ($M_w \leq 6.4$), *QuakeUp* has shown effectiveness for offshore events in areas with low instrumentation density.

List of Acronyms:

AS: Aftershock

EEWS: Earthquake Early Warning System

FA: False Alert

FOR: Foreshock

GMPE: Ground Motion Prediction Equation

IGN: *Instituto Geográfico Nacional*

IMM: Instrumental Intensity

IMR: Ibero-Maghrebian Region

IPMA: Instituto Português do Mar e da Atmosfera

MA: Missed Alert

MS: Main Shock

OT: Origin Time

PDZ: Potential Damage Zone

PGV: Peak Ground Velocity

SA: Successful Alerts

SNA: Successful No-Alerts

TFA: Time of the First Alert

UCM: Universidad Complutense de Madrid

WM: Western Mediterranean

Data and resources

The waveform data used for the playback analysis in the study came are from stations belonging to IGN (https://doi.org/10.7914/SN/ES), WM (https://doi.org/10.14470/JZ581150), and IPMA (https://doi.org/10.7914/SN/PM) seismic networks. All the waveforms used for the calibration of the empirical laws and the GMPE came from the same seismic networks. These records were processed (mean value corrected, linear trend removed, P-wave identified, and divided by sensitivity) using Seismic Analysis Code, SAC (Version 101.6a, academic licence, available at http://ds.iris.edu/ds/nodes/dmc/software/downloads/sac/, last accessed, June 2024). The hypocentral locations and M_w of selected earthquakes (Table S1, S4 and S5) came from published sources listed in the references and the IGN Seismic Catalog (https://doi.org/10.7419/162.03.2022; last accessed, September 2024).

The used EEWS software (*QuakeUp*) can be found at https://doi.org/10.5281/zenodo.11103858 (last accessed, June 2024). The grids to perform the location were calculated using the software NLLoc by A. Lomax, available at https://github.com/alomax/NonLinLoc (last accessed, June 2024), with a velocity model specific for the studied area (Carreño *et al.,* 2003).

The supplemental material also includes details on databases, empirical laws for magnitude and PGV prediction, GMPE for the IMR, differences in source parameters, and impact prediction maps for the mainshock.

The MATLAB code (24.1.0.2578822 (R2024a) Update 2, academic licence) has been used for the calibration of the empirical laws and the GMPE. The same software was used to produce Figs. 3, 4,5,7, S2, S4 S6 and S7. Figures 1, 6, 8, S1, S3, S5 and S8 were made using Generic Mapping Tools Version 6.5.0 (https://docs.generic-mapping-tools.org/6.5/devdocs/team.html, last accessed, September 2024)

Declaration of Competing Interest

The authors acknowledge there are no conflicts of interest recorded.

Acknowledgments

The research was funded by the Spanish Ministry of Economy and Competitiveness (Project Number PID2021-122662OB-I00), the Italian Ministry of University and Research through the National Operative Program PON-AIM AIM1834927 and the Geo-INQUIRE project funded by the European Commission (HORIZON-INFRA-2021-SERV-01, Project Number 101058518).

References

Alcik H., O. Ozel, Y. Wu, N.M. Ozel and M. Erdik (2011). An alternative approach for the Istanbul earthquake early warning system. *Soil Dynamics and Earthquake Engineering* 31(2):181–7. https://doi.org/10.1016/j.soildyn.2010.03.007

Allen, R. M., and Kanamori, H. (2003). The potential for earthquake early warning in southern California. *Science*, *300*(5620), 786-789.

Allen, R. M., and Melgar, D. (2019). Earthquake early warning: Advances, scientific challenges, and societal needs. *Annual Review of Earth and Planetary Sciences*, 47(1), 361-388. https://doi.org/10.1146/annurev-earth-053018-060457

Böse, M., T. H. Heaton, and E. Hauksson, (2012). Real-time finite fault rupture detector (FinDer) for large earthquakes. *Geophysical Journal International*, 191(2), 803-812. https://doi.org/10.1111/j.1365-246X.2012.05657.x

Böse, M., R. M. Allen, H. Brown, G. Gua, M. Fischer, E. Hauksson, T. Heaten, M. Hellweg, M. Liukis, D. Neuhauser, P. Maechling, K. Solanki, M. Vinci, I. Henson, O. Khainovski, S. Kuyuk, M. Carpio, M.-A. Meier & T. Jordan (2013). CISN ShakeAlert—An earthquake early warning demonstration system for California, Early Warning for Geological Disasters: Scientific Methods and Current Practice, 49-69, F. Wenzel and J. Zschau (Editors), Springer, Berlin, Heidelberg. https://doi.org/10.1007/978-3-642-12233-0_3

Buforn, E., A. Udías, and C. Pro (2015). Large Earthquakes at the Ibero-Maghrebian Region: Basis for an EEWS. *Pure Appl. Geophys*. 172 (9), 2387–2396. https://doi.org/10.1007/s00024-014-0954-0

Buforn, E., C. Pro, C. Sanz de Galdeano, , J.V. Cantavella, S.Cesca, B. Caldeira, A. Udías, and M. Mattesini (2017). The 2016 south Alboran earthquake (Mw = 6.4): A reactivation of the Ibero-Maghrebian region? *Tectonophysics* 712-713, 704-715. http://dx.doi.org/10.1016/j.tecto.2017.06.033

Carranza, M., E. Buforn, S. Colombelli and A. Zollo (2013). Earthquake early warning for southern Iberia: A P wave threshold-based approach. *Geophysical Research Letters* 40, 4588-4593. https://doi.org/10.1002/grl.50903

Carranza, M. (2016). Sistema de alerta sísmica temprana para el sur de la Península Ibérica: determinación de los parámetros de la alerta. *Ph. D. Thesis*. Madrid: Universidad Complutense de Madrid (in Spanish).

Carranza, M., E. Buforn, and A. Zollo (2017). Performance of a Network-Based Earthquake Early Warning System in the Ibero-Maghrebian Region. *Seismological Research Letters* 88 (6): 1499–1507. https://doi.org/10.1785/0220170081

Carranza, M., M. Mattesini, E. Buforn, A. Zollo and I. Torrego (2021). Four years of earthquake early warning in Southern Iberia: 2016–2019. *Frontiers in Earth Science*, 9, 696191. https://doi.org/10.3389/feart.2021.696191

Carreño, E., C. López, B. Bravo, P. Expósito, E. Gurría and O. García (2003). Sismicidad de la Península Ibérica en la época instrumental: 1985-2002. *Física de la Tierra 15, 73-91 (in Spanish)*. https://revistas.ucm.es/index.php/FITE/article/view/FITE0303110073A

Caruso, A., S. Colombelli, L. Elia, M. Picozzi and A. Zollo (2017). An onsite alert level early warning system for Italy. *Journal of Geophysical Research*: *Solid Earth*, 122. https://doi.org/10.1002/2016JB01340

Chamoli, B. P., A. Kumar, D.Y. Chen, A. Gairola, R.S. Jakka, B. Pandey, P. Kumar, and G. Rathore (2019). A Prototype Earthquake Early Warning System for Northern India. *Journal of Earthquake Engineering*, 25(12), 2455–2473. https://doi.org/10.1080/13632469.2019.1625828

Clinton, J., A. Zollo, A. Marmureanu, C. Zulfikar, and S. Parolai, (2016). State-of-the art and future of earthquake early warning in the European region. *Bulletin of Earthquake Engineering*, 14, 2441-2458. https://doi.org/10.1007/s10518-016-9922-7

Espinosa-Aranda, J. M, A. Jimenez, G. Ibarrola, F. Alcantar, A. Aguilar, M. Inostroza and S. Maldonado. (1995). Mexico City Seismic Alert System. *Seismological Research Letters* 66, 42-53.

Faenza, L. and A. Michelini, (2010). Regression analysis of MCS intensity and ground motion parameters in Italy and its application in ShakeMap. *Geophysical Journal International*, *180*(3), 1138-1152. https://doi.org/10.1111/j.1365-246X.2009.04467.x

Grünthal, G. (1998). European Macroseismic Scale 1998. *Cahiers du Centre European de Geodynamique et de Seismologie* (Vol. **15**). European Centre for Geodynamics and Seismology: Luxembourg City, Luxembourg

Gràcia, E., I. Grevemeyer, R. Bartolomé, H. Perea, S. Martínez-Loriente, L. Gómez de la Peña, A. Villaseñor, Y. Klinger, C. Lo Iacono, S. Diez, A. Calahorrano, M. Camafort, S. Costa, E. d'Acremont, A. Rabaute and C.R. Ranero (2019). Earthquake crisis unveils the growth of an incipient continental fault system. *Nature Communications* 10, 3482, https://doi.org/10.1038/s41467-019-11064-5

Hoshiba, M., O. Kamigaichi, M. Saito, S. Tsukada and N. Hamada (2008). Earthquake Early Warning Starts Nationwide in Japan. *EOS, Transactions American Geophysical Union*, 89 https://doi.org/10.1029/2008EO080001

Hsiao, N.C., Y.M. Wu, L. Zhao, D.Y. Chen, W.T. Huang, K.H. Kuo, T.C. Shin and P.L. Leu (2011). A new prototype system for earthquake early warning in Taiwan, *Soil Dynamics and Earthquake Engineering,* 31(2), 201-208. https://doi.org/10.1016/j.soildyn.2010.01.008

Instituto Geografico Nacional, Spain. (1999). Spanish Digital Seismic Network [Data set]. International Federation of Digital Seismograph Networks. https://doi.org/10.7914/SN/ES

Instituto Geográfico Nacional (2013). Actualización de mapas de peligrosidad sísmica de España 2012. Centro Nacional de Información Geográfica y Dirección General del Instituto Geográfico Nacional, Madrid (España), (in Spanish).

Instituto Português do Mar e da Atmosfera, I.P. (2006). Portuguese National Seismic Network [Data set]. International Federation of Digital Seismograph Networks. https://doi.org/10.7914/SN/PM

Lomax, A., C. Satriano, and M. Vassallo (2012). Automatic picker developments and optimization: FilterPicker - A robust, broadband picker for real-time seismic monitoring and earthquake early-warning. *Seismological Research Letters*, 83(3), 531–540. https://doi.org/10.1785/gssrl.83.3.531

Massin, F., J. Clinton and M. Böse (2021). Status of Earthquake Early Warning in Switzerland. *Frontiers in Earth Science*. 9:707654. https://doi.org/10.3389/feart.2021.707654

Medina, M., R. Sanchez, S. Riquelme, M.C. Flores, P. Koch, F. Bravo, S. Barrientos, I. Henson, A. Chung, D. Melgar, C. Mpodozis, M. Hellweg and R. Allen (2022). An Earthquake Early Warning System for Northern Chile Based on ElarmS-3. *Seismological Research Letters* 93 (6): 3337–3347.https://doi.org/10.1785/0220210331

Mézcua, J. and J.M. Martínez Solares (1983). Sismicidad del Área Ibero-Mogrebí. Instituto Geográfico Nacional, Madrid, (in Spanish).

Picozzi, M., S. Colombelli, A. Zollo, M. Carranza and E. Buforn, (2015). A Threshold-Based Earthquake Early-Warning System for Offshore Events in Southern Iberia. *Pure and Applied Geophysics*, *172*, 2467-2480. https://doi.org/10.1007/s00024-014-1009-2

Peng, H., Z. Wu, Y.M. Wu, S. Yu, D. Zhang and W. Huang. (2011). Developing a prototype earthquake early warning system in the Beijing capital region, *Seismological Research Letters* 82(3): 394–403. https://doi.org/10.1785/gssrl.82.3.394

Pro, C., E. Buforn, S. Cesca, C. Sanz de Galdeano and A. Udías (2014). Rupture process of the Lorca (southeast Spain) 11 May 2011 (M_w = 5.1) earthquake. *Journal of Seismology*, 18. 481-495. https://doi.org/10.1007/s10950-014-9421-8

Rea, R., S. Colombelli, L. Elia and A. Zollo (2024). Retrospective performance analysis of a ground shaking early warning system for the 2023 Turkey–Syria earthquake. *Communications Earth & Environment,* 5, 332. https://doi.org/10.1038/s43247-024-01507-3

San Fernando Royal Naval Observatory (ROA), Universidad Complutense De Madrid (UCM), Helmholtz-Zentrum Potsdam Deutsches GeoForschungsZentrum (GFZ), Universidade De Évora (UEVORA, Portugal), & Institute Scientifique of Rabat (ISRABAT, Morocco). (1996). The

Western Mediterranean Broand-Band seismic Network [Data set]. GFZ Data Services. https://doi.org/10.14470/JZ581150

Satriano, C., A. Lomax, and A. Zollo (2008). Real-time evolutionary earthquake location for seismic early warning. *Bulletin of the Seismological Society of America*, *98*(3), 1482-1494. https://doi.org/10.1785/0120060159

Satriano, C., L. Elia, C. Martino, M. Lancieri, A. Zollo and G. Iannaccone (2011). PRESTo, the earthquake early warning system for southern Italy: Concepts, capabilities and future perspectives, *Soil Dynamics and Earthquake Engineering,* 31(2), 137-153. https://doi.org/10.1016/j.soildyn.2010.06.008

Sheen, D-H., J.H. Park, H.C. Chi, E.H. Hwang, I.S. Lim, Y. Jeong Seong and J. Pak (2017). The first stage of an earthquake early warning system in South Korea. *Seismological Research Letters*, 88(6), 1491-1498. https://doi.org/10.1785/0220170062

Stich, D., F. Mancilla, D. Baumont, and J. Morales (2005), Source analysis of the M_w 6.3 2004 Al Hoceima earthquake (Morocco) using regional apparent source time functions, *Journal of Geophysical Research*, 110, B06306. https://doi.org/10.1029/2004JB003366

Suárez, G., J. M. Espinosa-Aranda, A. Cuéllar, A. Uribe, G. Ibarrola, A. García, R. Islas and L. Camarillo (2021). Evaluation of the Seismic Alert System of Mexico (SASMEX) during the June 23, 2020, Oaxaca Earthquake (Mw 7.4). *Natural hazards,* 108(3), 3085–3098. https://doi.org/10.1007/s11069-021-04815-5

Udías, A. and E. Buforn (2018). Principles of seismology. Cambridge University Press.

Wang, Y., S. Colombelli, A. Zollo and S. Li (2024). Near-epicenter-based partial matching crossover algorithm for estimating the strong-shaking zone of large earthquakes. Bulletin of Earthquake Engineering, 22(11), 5545-5570. https://doi.org/10.1007/s10518-024-01981-2

Worden, C. B., D. J. Wald, T. I. Allen, K. Lin, D. Garcia and G. Cua (2010). A revised ground-motion and intensity interpolation scheme for ShakeMap. *Bulletin of the Seismological Society of America*, 100(6), 3083–3096. https://doi.org/10.1785/0120100101

Zollo, A., S. Colombelli, A. Caruso and L. Elia (2023). An evolutionary shaking-forecast-based earthquake early warning method. *Earth and Space Science*, 10, e2022EA002657. https://doi.org/10.1029/2022EA002657

Full mailing address for each author:

L. Escudero, M. Mattesini and E. Buforn

Departamento de Física de la Tierra y Astrofísica, Facultad de Ciencias Físicas

Universidad Complutense de Madrid

Plaza de Ciencias 1

28040 Madrid, Spain

A. Zollo, R. Rea, L. Elia and S. Colombelli

Dipartimento di Fisica *"Ettore Pancini"*

Università degli Studi di Napoli Federico II

Via Cinthia, 21

80126 Naples, Italy

Table 1.- Coefficients for Eq. (1) obtained for the three parameters P_a, P_v y P_d using a 20 s P-wave time window. The last column shows the standard deviation (σ) of the adjustments. The subscript x indicates either a, d, or v.

	A_x	B_x	C_x	σ_x
P_a (cm/s2)	2.3 ± 0.5	0.73 ± 0.06	1.6 ± 0.2	0.52
P_v (cm/s)	2.7 ± 0.3	0.88 ± 0.04	1.9 ± 0.1	0.41
P_d (cm)	3.4 ± 0.4	0.81 ± 0.04	1.9 ± 0.2	0.46

Table 2.- Coefficients for Eq. (2) obtained for the three parameters P_a, P_v y P_d using a 20 s P-wave time window. The last column shows the standard deviation (σ) of the adjustments. The subscript x indicates either a, d, or v.

	A'_x	B'_x	σ'_x
P_a (cm/s2)	-0.60 ± 0.07	0.90 ± 0.05	0.53
P_v (cm/s)	0.64 ± 0.09	0.98 ± 0.04	0.41
P_d (cm)	1.5 ± 0.1	0.93 ± 0.04	0.44

Figure 1: Epicenters of the 2016 Alboran seismic series: main shock (MS, black star), foreshock (FOR) and aftershocks (AS) with $M_w \geq 5$ (gray circles) together with their focal mechanism (Buforn *et al.*, 2017). Triangles are the seismic stations used (blue WM, red IGN and green IPMA). 1: 1755 Lisbon earthquake, 2: 1829 Torrevieja earthquake, 3: 1884 Arenas del Rey earthquake, 4: 2004 Al Hoceima, M_w 6.4, 5: 2011 Lorca, M_w 5.1. SVC: Cape St. Vincent.

Figure 2: Block diagram of the method. The left panel shows on-site processing, including PGV prediction, while the center panel illustrates focal parameter estimations and network-based PGV predictions. These are combined for a refined, real-time shakemap construction, shown in the right panel, along with the dissemination of alerts to target sites. This figure has been modified from Zollo *et al.,* (2023) for its specific application in the IMR.

Figure 3: a) M_w versus P_x $(x = a, v, d)$ for a 20 s P-wave time windows of the selected events (Table S1). The hypocentral distance is marked by the vertical colorbar. A hypocentral distance of 350 km has been fixed to show the interpolated law (solid line) and its uncertainty (dashed line). **b)** PGV versus P_x $(x = a, v, d)$ for a 20 s P-wave time windows. The interpolation law (solid line) and its uncertainty (dashed line) are also shown, along with the vertical M_w colorbar.

Figure 4: Time differences between the focal parameters in this study and those of Buforn *et al.,* (2017) for the main shock: **a)** origin time (ΔOT), **b)** epicenter location (ΔR) and **c)** depth (Δh). **d)** Time evolution of the earthquake M_w (blue curve) and of the magnitude calculated at each recording station (gray curves). At the bottom-left, the histogram shows the estimated M_w recorded at the stations at the end of the simulation.

Figure 5: Lead-time at each station versus the epicentral distance. a) Time after OT in which the I_{MM}^{pred} exceeds the threshold I_{MM}^{thres}=IV (Faenza & Michelini, 2010) (green circles). Time after

OT in which I_{MM}^{obs} exceeded the same threshold (red circles). The segment lengths connecting the points represent the lead-time. **b)** Same as a) but using the threshold I_{MM}^{thres}=V (Faenza & Michelini, 2010).

Figure 6: Impact prediction. Performance of the system at recording stations in terms of SA (light green), SNA (dark green), MA (red) and FA (yellow). Each panel reports three different times after OT, arranged in a clockwise direction. The threshold I_{MM}^{thres} =IV (Faenza & Michelini, 2010) was considered. The yellow and red circles represent the P-wave and the S-wave fronts, respectively, while the epicenter is shown (black star). The Alboran Sea (A.S.) and Gulf of Cadiz (G.C.) regions are highlighted.

Figure 7: Histograms of the differences ΔOT **(a)**, ΔR **(b)**, Δh **(c)**, ΔM_w **(d)** and ΔI_{MM} **(e)** at two different times after OT: T_{FIRST} (right column) and T_{STB} (left column).

Figure 8: a-c) P-wave based early shake maps at different times after OT (reported in each panel) based on the law of Faenza & Michelini (2010). The stations are represented by gray triangles, and the black star indicates the epicenter of the main shock. The contour line of the PDZ considering I_{MM}^{thres}=V (Faenza & Michelini, 2010), is shown (black line). **d)** Intensity map (EMS-98) for the main shock. The felt reports of the IGN are used. 1: Al Hoceima 2: Imzouren 3: Melilla 4: Adra 5: Salobreña.

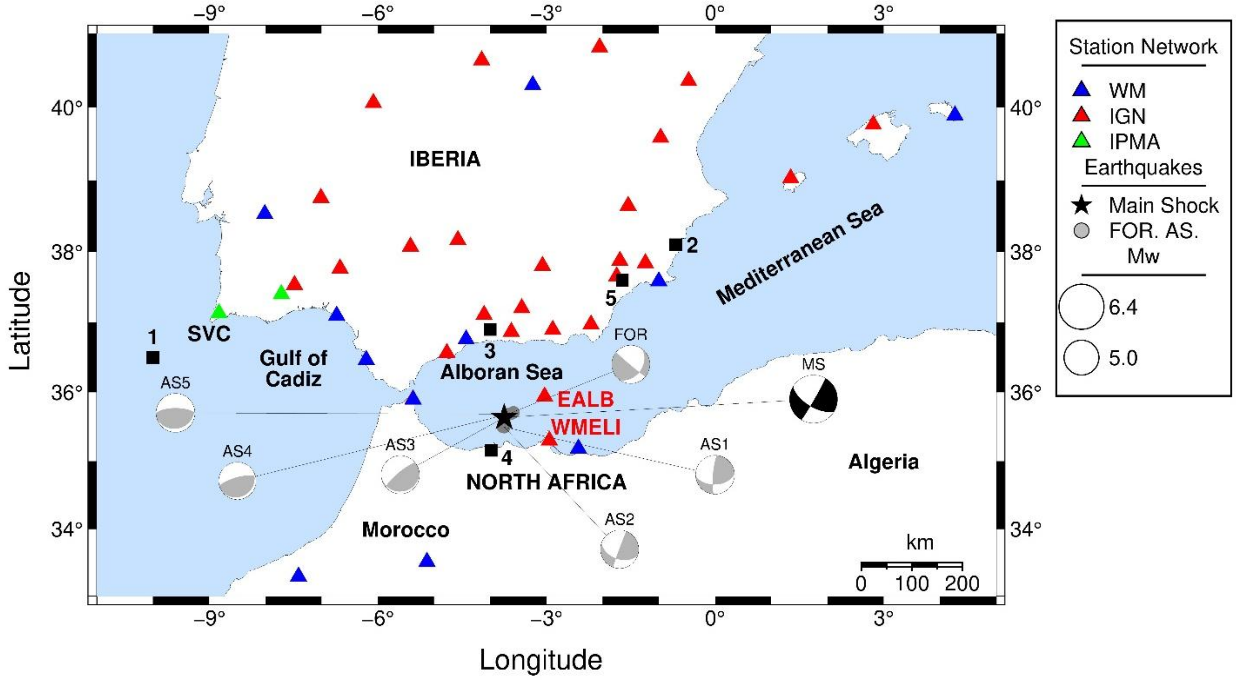

Figure 1: Epicenters of the 2016 Alboran seismic series: main shock (MS, black star), foreshock (FOR) and aftershocks (AS) with $M_w \geq 5$ (gray circles) together with their focal mechanism (Buforn *et al.*, 2017). Triangles are the seismic stations used (blue WM, red IGN and green IPMA). 1: 1755 Lisbon earthquake, 2: 1829 Torrevieja earthquake, 3: 1884 Arenas del Rey earthquake, 4: 2004 Al Hoceima, M_w 6.4, 5: 2011 Lorca, M_w 5.1. SVC: Cape St. Vincent.

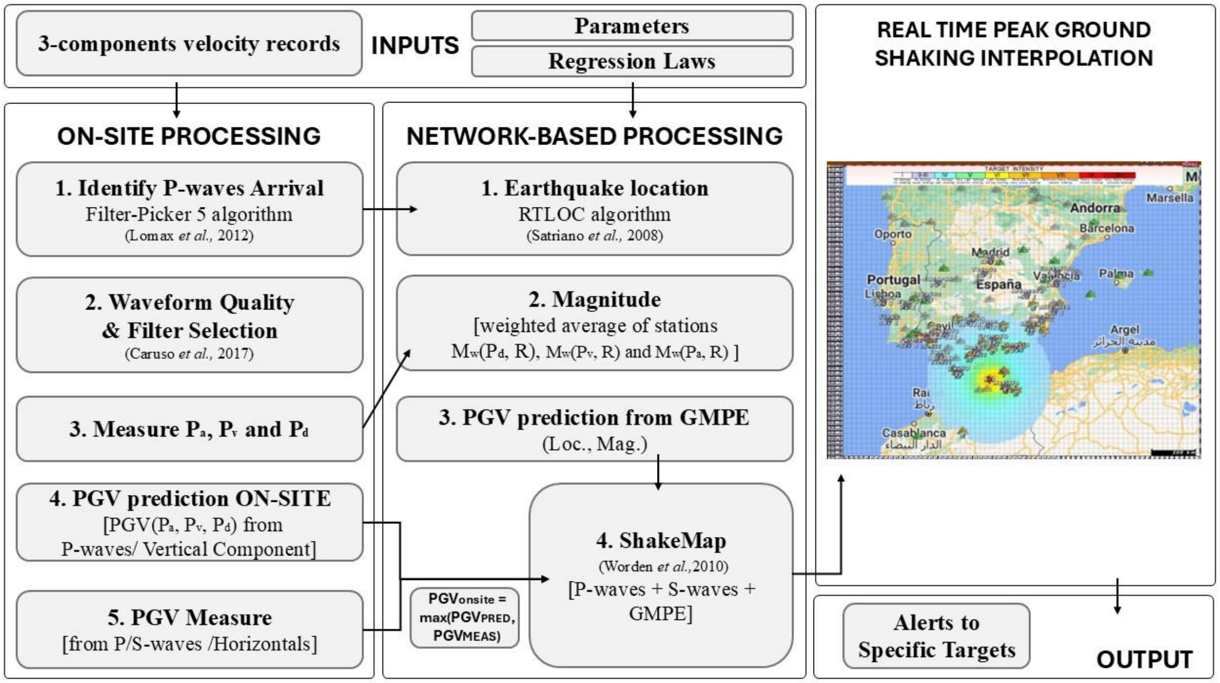

Figure 2: Block diagram of the method. The left panel shows on-site processing, including PGV prediction, while the center panel illustrates focal parameter estimations and network-based PGV predictions. These are combined for a refined, real-time shakemap construction, shown in the right panel, along with the dissemination of alerts to target sites. This figure has been modified from Zollo *et al.,* (2023) for its specific application in the IMR.

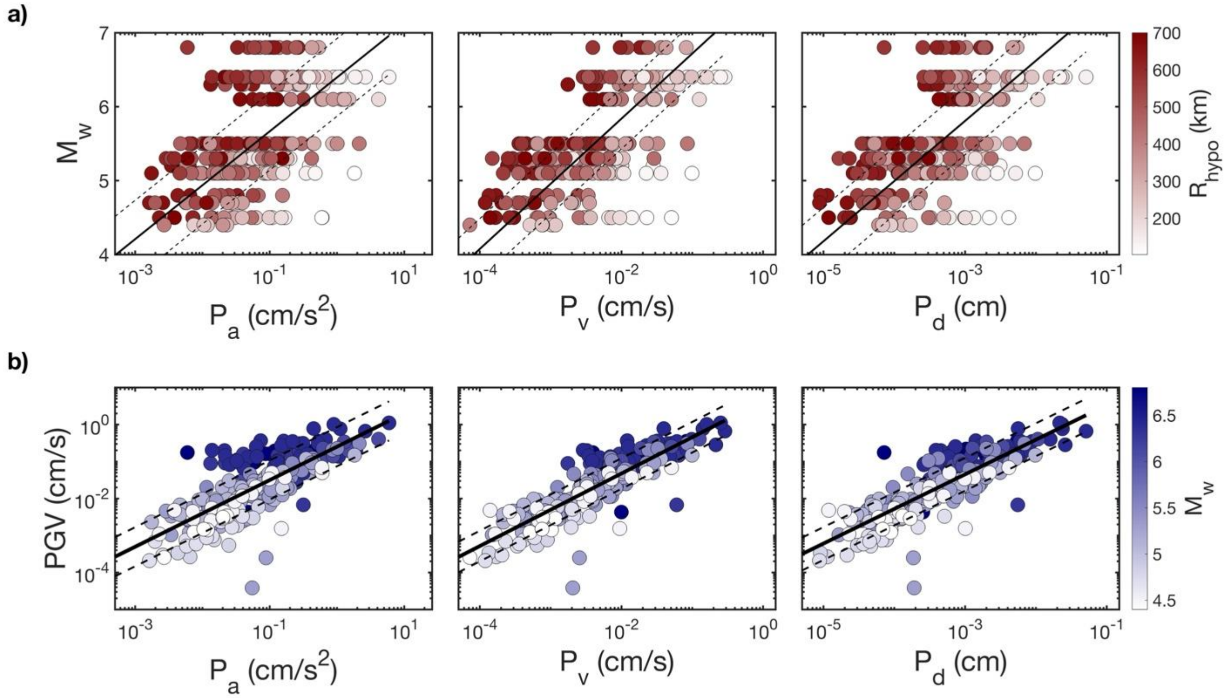

Figure 3: a) M_w versus P_x $(x = a, v, d)$ for a 20 s P-wave time windows of the selected events (Table S1). The hypocentral distance is marked by the vertical colorbar. A hypocentral distance of 350 km has been fixed to show the interpolated law (solid line) and its uncertainty (dashed line). **b)** PGV versus P_x $(x = a, v, d)$ for a 20 s P-wave time windows. The interpolation law (solid line) and its uncertainty (dashed line) are also shown, along with the vertical M_w colorbar.

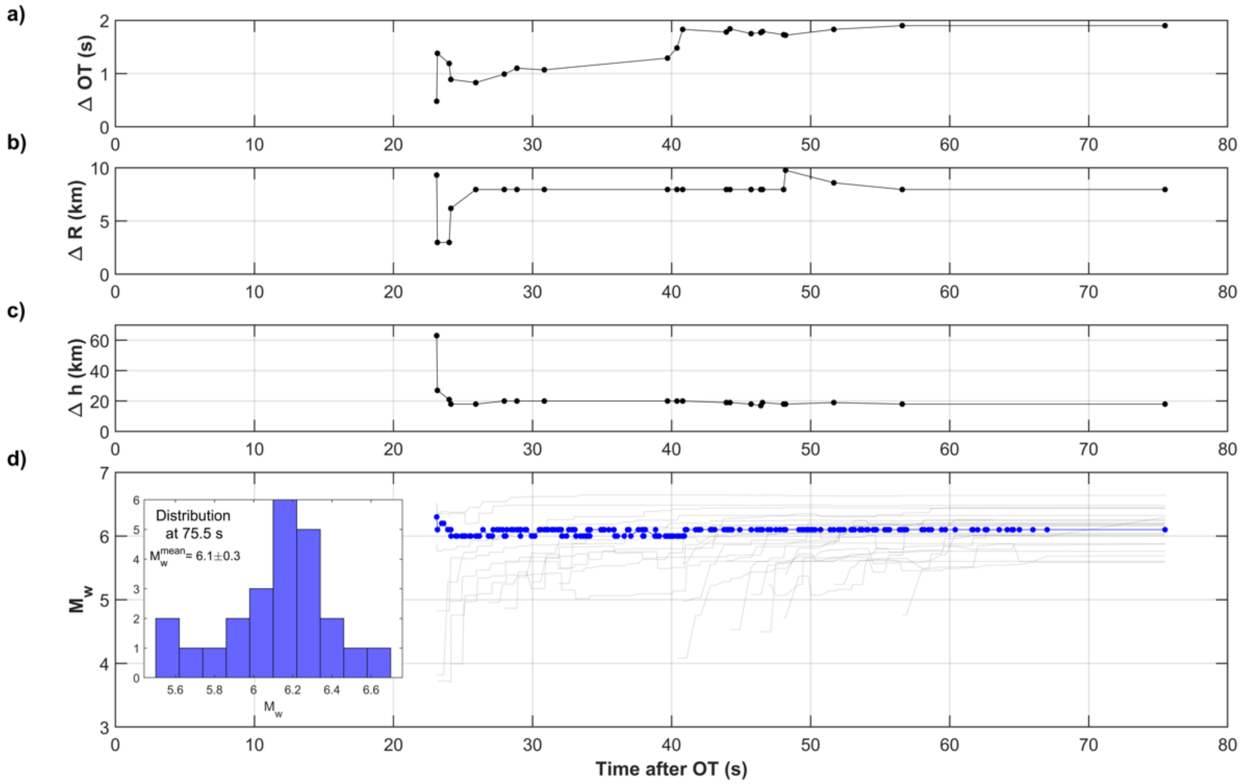

Figure 4: Time differences between the focal parameters in this study and those of Buforn *et al.,* (2017) for the main shock: **a)** origin time (ΔOT), **b)** epicenter location (ΔR) and **c)** depth (Δh). **d)** Time evolution of the earthquake M_w (blue curve) and of the magnitude calculated at each recording station (gray curves). At the bottom-left, the histogram shows the estimated M_w recorded at the stations at the end of the simulation.

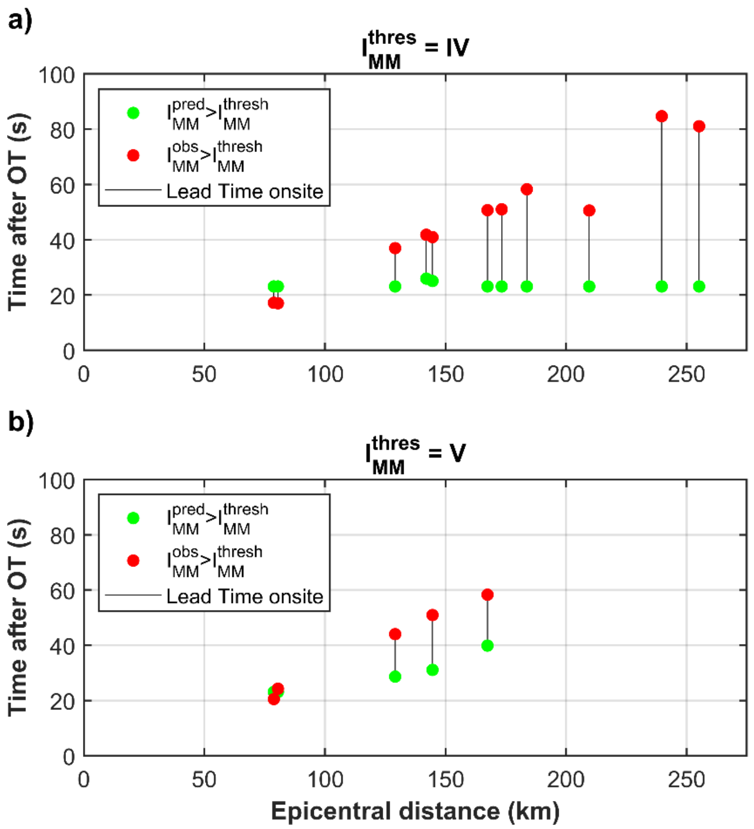

Figure 5: Lead-time at each station versus the epicentral distance. a) Time after OT in which the I_{MM}^{pred} exceeds the threshold I_{MM}^{thres}=IV (Faenza & Michelini, 2010) (green circles). Time after OT in which I_{MM}^{obs} exceeded the same threshold (red circles). The segment lengths connecting the points represent the lead-time. **b)** Same as a) but using the threshold I_{MM}^{thres}=V (Faenza & Michelini, 2010).

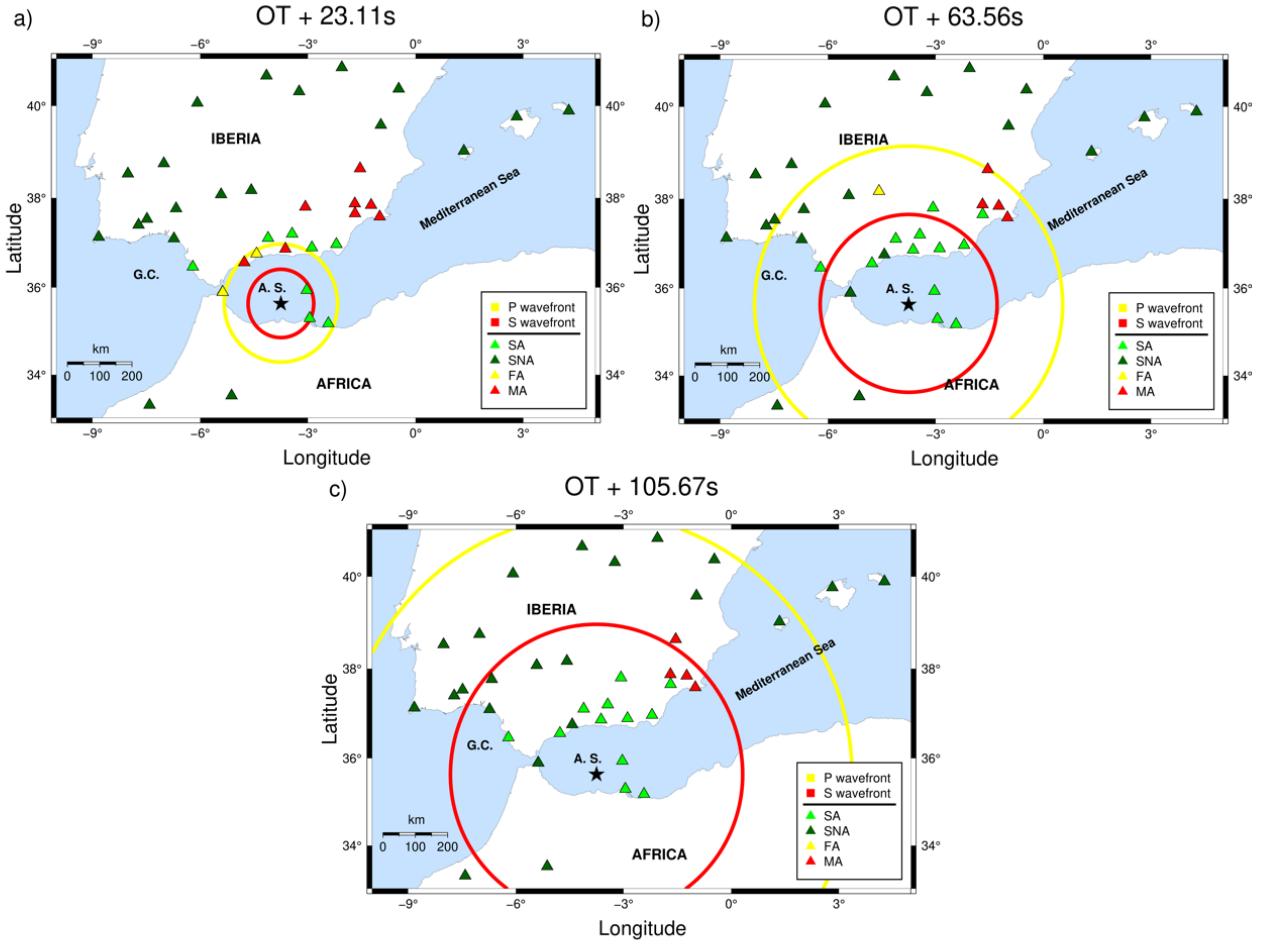

Figure 6: Impact prediction. Performance of *QuakeUp* at recording stations in terms of SA (light green), SNA (dark green), MA (red) and FA (yellow). Each panel reports three different times after OT, arranged in a clockwise direction. The threshold I_{MM}^{thres} =IV (Faenza & Michelini, 2010) was considered. The yellow and red circles represent the P-wave and the S-wave fronts, respectively, while the epicenter is shown (black star). The Alboran Sea (A.S.) and Gulf of Cadiz (G.C.) regions are highlighted.

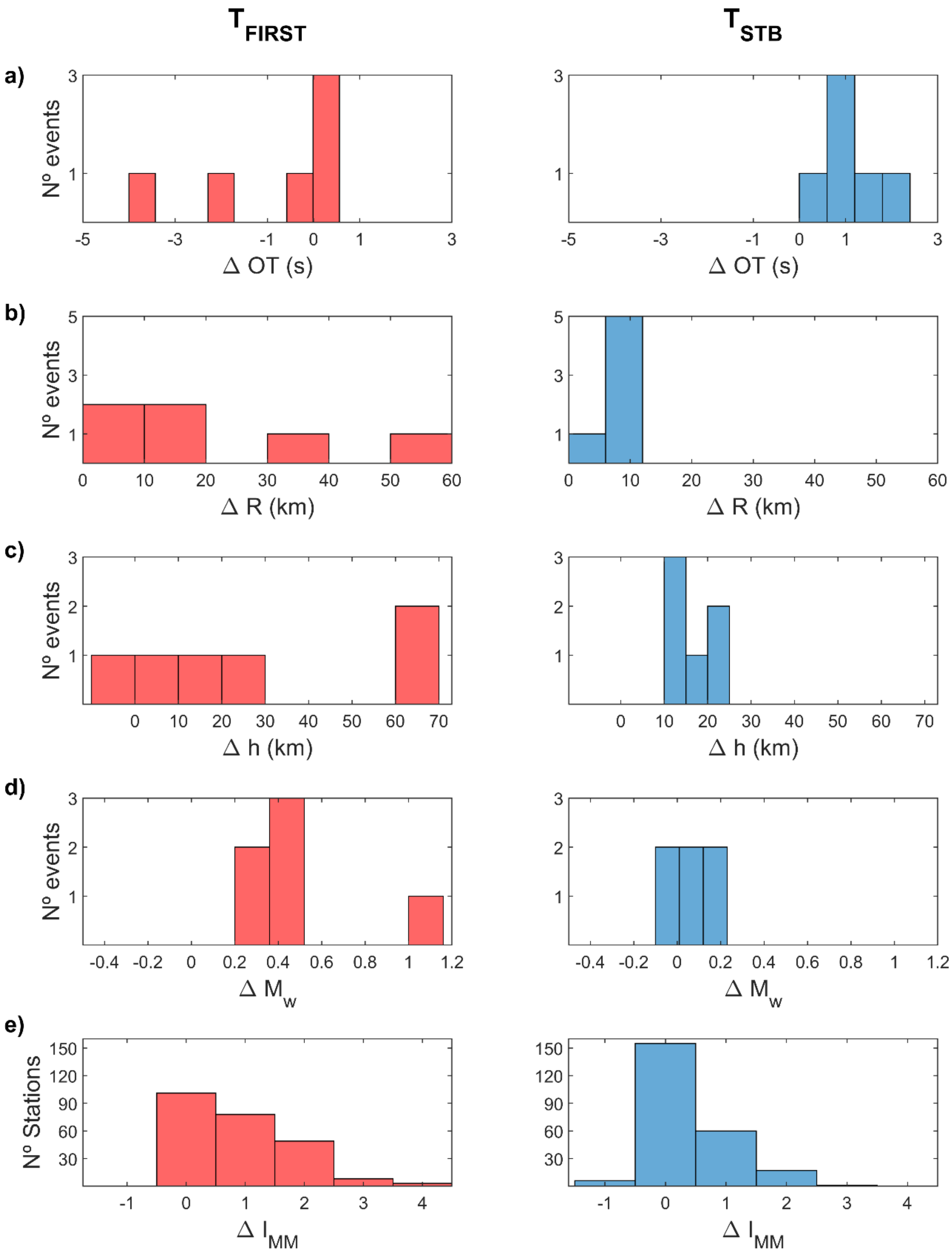

Figure 7: Histograms of the differences ΔOT **(a)**, ΔR **(b)**, Δh **(c)**, ΔM_w **(d)** and ΔI_{MM} **(e)** at two different times after OT: T_{FIRST} (right column) and T_{STB} (left column).

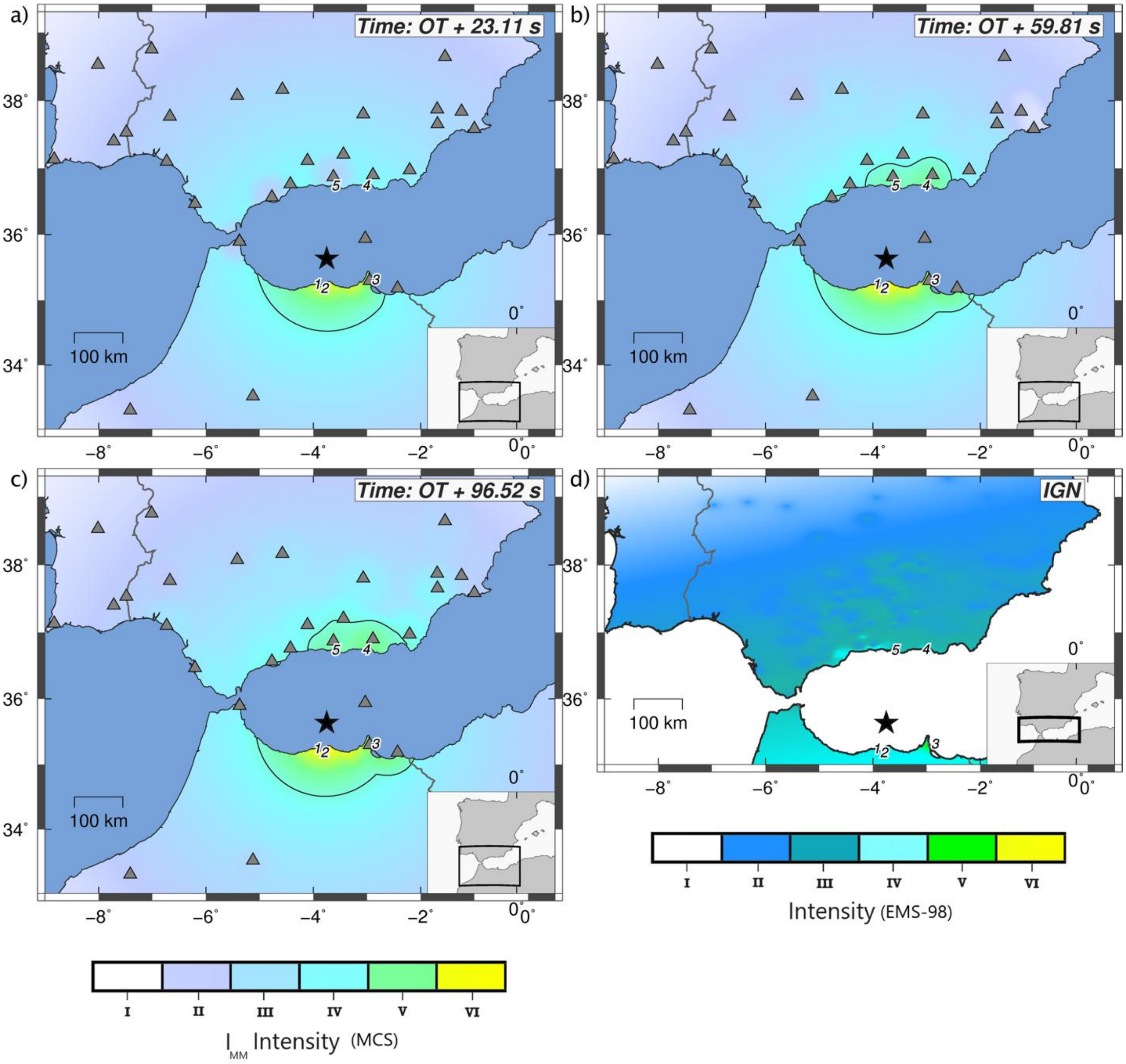

Figure 8: a-c) P-wave based early shake maps at different times after OT (reported in each panel) based on the law of Faenza & Michelini (2010). The stations are represented by gray triangles, and the black star indicates the epicenter of the main shock. The contour line of the PDZ considering I_{MM}^{thres}=V (Faenza & Michelini, 2010), is shown (black line). **d)** Intensity map (EMS-98) for the main shock. The felt reports of the IGN are used. 1: Al-Hoceima 2: Imzouren 3: Melilla 4: Adra 5: Salobreña.